https://doi.org/10.1093/mnras/stab3087

Downloaded from https://academic.oup.com/mnras/article/509/2/1736/6409155 by College of Charleston user on 03 December 202-

Advance Access publication 2021 October 25

Evolution of accretion disc reflection spectra due to a Type I X-ray burst

J. Speicher [®], ¹★ D. R. Ballantyne [®]1 and P. C. Fragile [®]2

Accepted 2021 October 19. Received 2021 October 6; in original form 2021 July 30

ABSTRACT

Irradiation of the accretion disc causes reflection signatures in the observed X-ray spectrum, encoding important information about the disc structure and density. A Type I X-ray burst will strongly irradiate the accretion disc and alter its properties. Previous numerical simulations predicted the evolution of the accretion disc due to an X-ray burst. Here, we process time-averaged simulation data of six time intervals to track changes in the reflection spectrum from the burst onset to just past its peak. We divide the reflecting region of the disc within $r \leq 50$ km into six to seven radial zones for every time interval and compute the reflection spectra for each zone. We integrate these reflection spectra to obtain a total reflection spectrum per time interval. The burst ionizes and heats the disc, which gradually weakens all emission lines. Compton scattering and bremsstrahlung rates increase in the disc during the burst rise, and the soft excess at <3 keV rises from ≈ 4 to ≈ 38 per cent of the total emission at the burst peak. A soft excess is expected to be ubiquitous in the reflection spectra of X-ray bursts. Structural disc changes such as inflation because of heating or drainage of the inner disc due to Poynting–Robertson drag affect the strength of the soft excess. Further studies on the dependence of the reflection spectrum characteristics to changes in the accretion disc during an X-ray burst may lead to probes of the disc geometry.

Key words: accretion, accretion discs – radiative transfer – stars: neutron – X-rays: binaries – X-rays: bursts.

1 INTRODUCTION

Reflection features are a common observable in the X-ray spectra of accreting compact objects of all mass scales (e.g. Nandra & Pounds 1994; Xu et al. 2020; Szanecki, Niedźwiecki & Zdziarski 2021). The most prominent reflection features are the Fe K α line at \approx 6–7 keV (e.g. George & Fabian 1991; Nandra & Pounds 1994; Fabian et al. 2000; Ballantyne & Ross 2002; for a review, see Miller 2007) and the so-called Compton hump above 10 keV (e.g. Lightman & White 1988; George & Fabian 1991). These features arise through reprocessed radiation. In binary systems, the reflection of radiation occurs primarily in the accretion disc (e.g. Cackett et al. 2010). Due to the dependence on the reflector properties, reflection features are a powerful tool to study the accretion disc (e.g. Ross & Fabian 1993, 2005; García, Kallman & Mushotzky 2011; García et al. 2020).

For neutron stars in low-mass X-ray binaries, the accretion disc is irradiated by a boundary layer (e.g. Inogamov & Sunyaev 1999; Popham & Sunyaev 2001; Inogamov & Sunyaev 2010; Ding, Chen & Qu 2021), corona (e.g. Galeev, Rosner & Vaiana 1979), and, for some systems, by a Type I X-ray burst. Neutron stars in low-mass X-ray binaries accrete matter, predominantly hydrogen and helium, from a donor star via Roche lobe overflow. The matter accumulates as an additional layer on the neutron star surface. This layer is subject to rising pressure and heats up until unstable nuclear burning sets off a conflagration detectable as an X-ray burst (for a review, see Lewin, van Paradijs & Taam 1993; Galloway & Keek 2021). During a burst, the neutron star emits large amounts of soft X-ray radiation,

* E-mail: juliasp@gatech.edu

which has detectable impacts on the neutron star environment (for a review, see Degenaar et al. 2018). The burst radiation Compton cools the corona and reduces its hard X-ray emission (e.g. Maccarone & Coppi 2003; Sánchez-Fernández et al. 2020; Speicher, Ballantyne & Malzac 2020). As the burst emission supersedes the coronal and boundary layer emission as the dominant radiation intercepting the accretion disc, its reflection spectrum will change likewise. During bursts, observations record a soft excess (e.g. in't Zand et al. 2013; Keek et al. 2018; Bult et al. 2019; Chen et al. 2019). In addition, Fe K and L lines may be detected during bursts (e.g. Strohmayer & Brown 2002; Degenaar et al. 2013; in't Zand et al. 2013; Keek et al. 2014a, 2017; Bult et al. 2019).

Time-resolved observations of Type I X-ray bursts are challenging due to their typically short duration of a few seconds (e.g. Keek et al. 2018; Bult et al. 2019), and are only now becoming more common with observatories such as *NICER* (Gendreau & Arzoumanian 2017). In the past, detailed time-resolved observations have been limited to longer bursts such as intermediate-duration bursts and superbursts. Keek et al. (2017) found a 1 keV emission line weakening with decreasing burst flux during an intermediate-duration burst. Evolving reflection features with receding burst flux have also been observed during superbursts (e.g. Strohmayer & Brown 2002; Ballantyne & Strohmayer 2004; Keek et al. (2014a,b). Ballantyne & Strohmayer (2004) and Keek et al. (2014b) used the changing reflection features to infer changes in the accretion disc structure, such as recession and inflation of the disc.

Recently, Fragile, Ballantyne & Blankenship (2020) simulated the time-dependent interaction of a thin accretion disc with a Type I X-ray burst during its rise. Their 2.5 s long simulations tracked the impact of a burst that peaked at 2.05 s with a peak luminosity

¹Center for Relativistic Astrophysics, School of Physics, Georgia Institute of Technology, 837 State Street, Atlanta, GA 30332-0430, USA

²Department of Physics & Astronomy, College of Charleston, 66 George Street, Charleston, SC 29424, USA

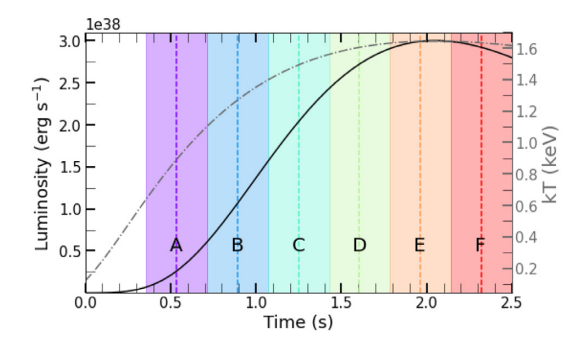


Figure 1. Time evolution of the burst luminosity and temperature from the Fragile et al. (2020) simulations. The burst luminosity (black solid line, equation 1) increases to a maximum of 3×10^{38} erg s⁻¹ at t = 2.05 s. The shaded regions labelled A–F mark the six 0.357 s long time intervals we analyse, which start at t = 0.357 s. Their mid-points used to calculate the luminosity per interval (equation 1) are marked by the dashed vertical lines. The burst blackbody temperature as seen from the disc is shown with the grey dot–dashed line (equation 2).

of 3×10^{38} erg s⁻¹. In their simulations, the burst radiation heated the disc, raising the disc temperature by half an order of magnitude. As a result, the disc height doubled and its surface density and optical depth decreased by an order of magnitude. Moreover, increased Poynting–Robertson (PR) drag increased the accretion rate by up to an order of magnitude, moving the disc inner radius by several km (see also Walker 1992; Worpel, Galloway & Price 2013, 2015).

With facilities such as *NICER*, time-resolved observations of Type I X-ray bursts are increasingly available (e.g. Keek et al. 2018). Their analysis requires an accurate understanding of the reflection spectrum evolution of the disc. Here, we present a simulation-based prediction of the evolving reflection spectrum due to the rise of a burst. We employ the simulation data by Fragile et al. (2020) to track the reflection spectrum as the Type I X-ray burst rises to its peak. In Section 2, we outline the calculations. We present the results in Section 3, which we discuss in Section 4. We state our conclusions in Section 5.

2 CALCULATIONS

We aim to demonstrate time-dependent changes of the reflection spectrum due to a Type I X-ray burst using the simulation data by Fragile et al. (2020). This section outlines the steps for processing the simulation data to obtain the needed input for our reflection spectra calculations.

In the simulation by Fragile et al. (2020), an azimuthally symmetric disc in hydrostatic equilibrium and with an initial mass accretion rate of $\dot{M} = 0.01 L_{\rm Edd}/c^2$, where $L_{\rm Edd}$ is the Eddington luminosity, is illuminated by an X-ray burst. For our calculations, we adopt the same burst luminosity L as Fragile et al. (2020), which is given by Norris et al. (2005),

$$L(t) = L_0 e^{2(\tau_1/\tau_2)^{1/2}} e^{-\frac{\tau_1}{t-t_s} - \frac{t-t_s}{\tau_2}}.$$
 (1)

In line with the simulations, $L_0 = 3 \times 10^{38}$ erg s⁻¹, $t_s = -0.4$ s, $\tau_1 = 6$ s, and $\tau_2 = 1$ s (Fragile et al. 2020). Fig. 1 depicts the burst luminosity evolution (black solid line). We focus on six 0.357 s long time intervals during the burst (A–F, shaded areas). The dashed vertical lines correspond to the interval mid-point, with which we calculate the luminosity in each time interval (equation 1).

We assume that the burst radiates as a blackbody and thus has a temperature $T_{\rm burst}$ as seen from the disc (Fig. 1, grey dot-dashed line).

$$T_{\text{burst}} = \left(\frac{L}{4\pi R_*^2 \sigma}\right)^{1/4} (1 + z_*)^{-1},$$
 (2)

where the gravitational redshift factor $(1 + z_*)$ is (Lewin et al. 1993)

$$1 + z_* = \left[1 - \frac{2GM}{R_*c^2}\right]^{-1/2},\tag{3}$$

 σ is the Stefan–Boltzmann constant and G the gravitational constant. Following Fragile et al. (2020), the neutron star mass is assumed to be $M=1.45~{\rm M}_{\odot}$ and its radius is $R_*=10.7~{\rm km}$.

For each time interval, we process the time-averaged, twodimensional simulation data by Fragile et al. (2020). The data are organized in 384 half-spherical shells, subdivided into 384 cells each. Each cell is associated with a gas density and a radiation flux vector. With the density, we calculate the hydrogen number density $n_{\rm H}$ and the optical depth τ due to Thomson scattering across a cell, assuming a mean molecular weight $\mu = 0.615$.

The irradiation of the burst sets the boundaries of the reflecting region. Due to the fluid-like nature of the radiation in the simulation, the burst flux flows across the high-density surface of the disc. We hence place the upper surface of our reflecting region where the average angle between the surface and radiation flux vectors is minimized. The average angles for our chosen surfaces are $\lesssim 3.4^\circ.$ To check whether the selected surfaces capture the entire reflecting region, we integrate from the equatorial plane upwards, and find that small deviations at the location of the upper surface change the integrated τ due to Thomson scattering by $\lesssim 3.5 \times 10^{-5}$ for all time intervals. Thus, the chosen surfaces are located in the atmosphere above the bulk of the disc.

Fig. 2 shows an example of the reflecting region for time interval C. The upper surface (black solid line) traces the disc atmosphere, defined using the minimization technique described above. We set the lower boundary (black solid line) so that the region fully captures the burst and the resulting temperature from X-ray heating stabilizes towards the bottom. This occurs at $\tau \approx 6$ for the time intervals A and B, $\tau \approx 8$ for interval C, at $\tau \approx 10$ for the intervals D and E, and at τ \approx 12 for interval F, if τ is integrated downwards starting at the upper surface. With the red dashed lines in Fig. 2, we constrain and divide the reflecting region into radial zones to capture radial variations in the simulation. There is a decrease in resolution in the simulated disc beyond $r \approx 64$ km and the outer regions have not reached equilibrium by the end of the simulation. Because the inner disc region is most resolved and contains the most significant structural disc changes, i.e. depletion of the innermost disc region due to PR drag and a change in height, we only consider the region within $r \lesssim 50$ km. As the burst proceeds, the inner accretion disc radius retracts, terminating the disc at $r \approx 19$ km in time interval E. Within these bounds, 19 km $\lesssim r \lesssim 50$ km, we create six static logarithmically spaced radial zones (1–6). We account for the retracting inner accretion disc radius with an additional radial zone (0) that starts at an inner accretion disc radius, $r \approx 15$ km, for intervals A-C. For interval D, we extend zone 1 to ≈18.4 km instead of creating an additional zone 0. For interval F, the inner accretion disc radius has retracted further and the inner boundary of zone 1 is $r \approx 19.2$ km. The gas inward of the innermost zone is optically thin and does not contribute to any reflection features.

For every radial zone in each time interval, we calculate a onedimensional vertical $n_{\rm H}$ profile. For this profile, we average $n_{\rm H}$ across all shells within a radial zone along a τ grid, consisting of 110,

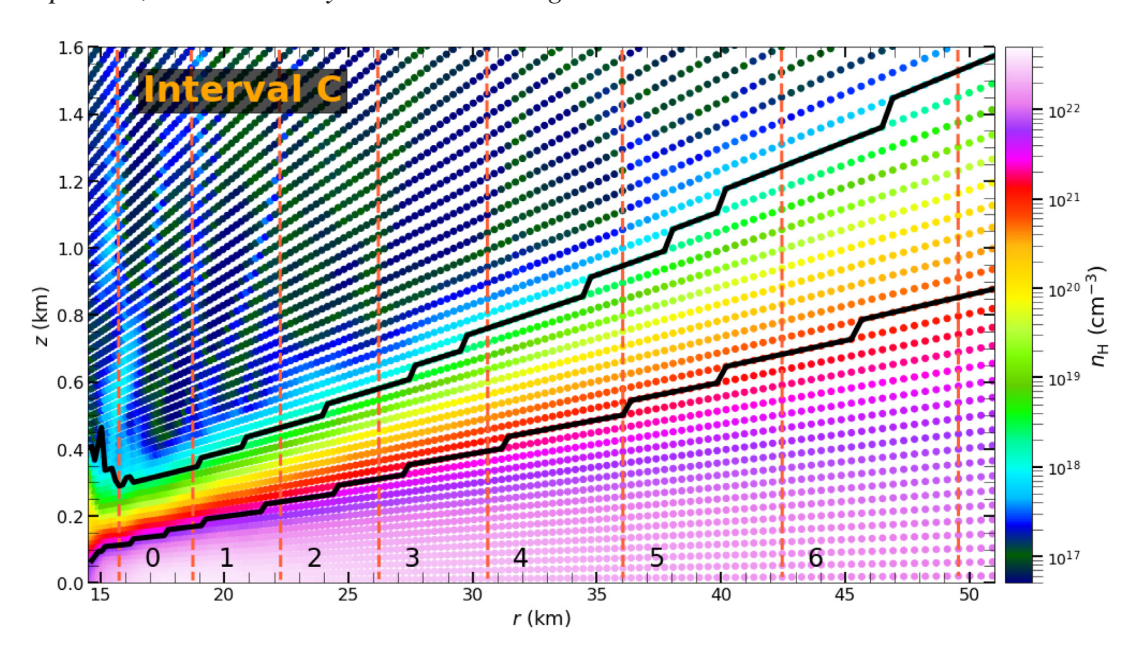


Figure 2. Gas density profile and reflecting region during time interval C. Upper and lower borders (black solid lines) constrain the reflecting region. The upper border follows the disc atmosphere as defined by the procedure described in Section 2. The lower border is placed far enough to ensure the capture of the entire burst radiation and is at $\tau \approx 8$, where τ is the optical depth due to Thomson scattering integrated from the upper surface. The disc is divided into seven radial zones (red dashed lines). Zone 0 is drained over time due to increased PR drag. Zones 1–6 are logarithmically spaced between $r \approx 19$ km and $r \approx 50$ km. They are of the same size for all time intervals. The gas inward of zone 0 is optically thin and does not contribute to any reflection features.

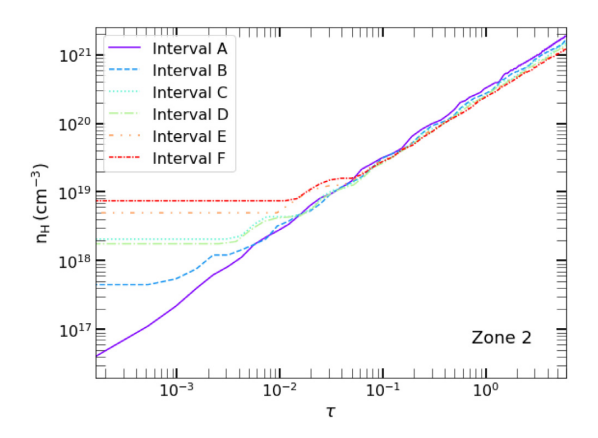


Figure 3. Vertical $n_{\rm H}$ profile for radial zone 2 for each time interval. The density (solid lines) increases within the reflecting region (Fig. 2). The density increases for the first $\tau \lesssim 5 \times 10^{-2}$ with time, but slightly decreases deeper within the reflection region. At $\tau \approx 1$, $n_{\rm H}$ decreases by a factor of ≈ 1.3 from the onset of the burst (interval A) to its peak (interval E). Due to the small overall $n_{\rm H}$ variations, the time dependence of $n_{\rm H}$ will not be the main driver of the reflection spectrum evolution.

logarithmically spaced entries that capture density variations within the reflecting region. The vertical $n_{\rm H}$ profile for the radial zone 2 is shown in Fig. 3 for each time interval (solid lines). The greatest $n_{\rm H}$ variations over time occur only for the first $\tau \lesssim 5 \times 10^{-2}$, over which $n_{\rm H}$ increases. The overall vertical $n_{\rm H}$ structure changes little, though. At $\tau \approx 1$, where the bulk of the radiation-disc interaction will occur, $n_{\rm H}$ reduces by a factor of ≈ 1.3 from the onset of the burst (interval A) to its peak (interval E). In contrast to that, the average burst flux irradiating radial zone 2 increases by a factor of ≈ 7 from interval A to interval E. Due to the small $n_{\rm H}$ decrease compared to the flux increase, we expect that the time dependence of $n_{\rm H}$ has a relatively

minor impact on the reflection spectra. Instead, the burst luminosity will be the main driver of the reflection spectrum evolution. This fact implies that constant density reflection models remain a good approximation to the emitted reflection spectrum (see Appendix A).

The burst irradiates the upper surface of each radial zone with an incidence angle of $\cos \theta = 1/\sqrt{3}$, following the one-stream approximation of radiative transer (Rybicki & Lightman 1986). In addition to the burst radiation, thermal radiation from the bulk of the disc is injected as diffuse radiation into the lower surface of each radial zone with temperature $T_{\rm th}$,

$$T_{\rm th} = \left(\frac{\bar{F}_{\rm th}}{\sigma}\right)^{1/4},\tag{4}$$

where \bar{F}_{th} is the corresponding average thermal flux, calculated from the simulations by averaging the flux magnitudes at the lower boundary of a radial zone in a time interval.

The vertical $n_{\rm H}$ profiles, the average burst, and thermal fluxes along with their temperatures are input into the code of Ballantyne, Ross & Fabian (2001), which calculates the angle-averaged restframe reflection spectrum for each radial zone and time interval. The burst irradiation propagates through the reflecting layer via a onestream approximation (Ross & Fabian 1993), while diffuse radiation is transferred via a Fokker-Planck equation (Ross, Weaver & McCray 1978). The photons heat and cool the gas via Compton scattering, bremsstrahlung, the photoelectric effect, recombination, and threebody interactions (Ross 1979). The code by Ballantyne et al. (2001) solves the equations of thermal and ionization equilibrium to determine the local temperature and fractional ionization in the τ grid defining the reflecting region (Ross & Fabian 1993). The code accounts for the ionization stages C V-VI, N VI-VII, O V-VIII, Mg IX-XII, Si XI-XIV, and Fe XVI-XXVI. We assume solar abundances. For each time interval, we integrate the reflection spectra of the radial zones by assuming that the upper surface forms the slant height of

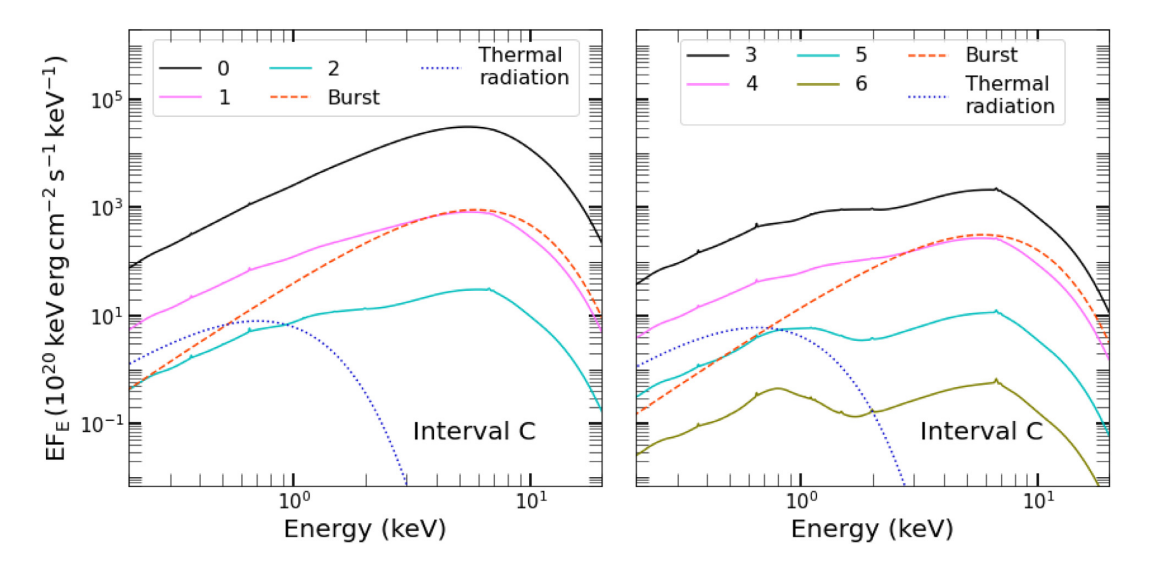


Figure 4. The solid lines show the reflection spectra of the radial zones, moving down, of interval C. For zone 1 (left-hand panel) and 4 (right-hand panel), we also plotted the burst (red dashed line) and the thermal emission (blue dotted line). The spectra were displaced by factors of 10 vertically for better visibility. The burst and thermal emission decrease with distance from the neutron star, causing the closest radial zones (left-hand panel) to be the most ionized. Emission lines are pronounced in the less ionized outer radial zones (right-hand panel), while closer radial zones exhibit more soft emission not attributed to the burst emission. Photoelectric absorption leads to an emission decrease at \approx 2 keV, most noticeable for radial zones 5 and 6 (right-hand panel).

joint conical frustums, and we calculate their lateral areas for each radial zone.

3 RESULTS

Fig. 4 shows the reflection spectra (solid lines) of all radial zones for time interval C. The spectra are displaced by factors of 10 vertically for better visibility. For radial zone 1 (left-hand panel) and 4 (right-hand panel), we also plot the burst emission (red dashed line) and the thermal radiation (blue dotted lines), which irradiate every radial zone from above and below, respectively. Comparing the spectra of the radial zones closest to the neutron star (0-2, lefthand panel) with the outer ones (3–6, right-hand panel), it becomes apparent that reflection features increase in strength with distance from the neutron star. While the reflection spectra 0-2 bear the closest resemblance to the incident burst radiation (red dashed line) with few, weak emission lines, spectra 3-6 feature more, stronger emission lines due to carbon, oxygen, and iron. In addition, the outermost spectra (5, 6) have a lower continuum at \approx 2 keV due to photoelectric absorption. The difference in reflection characteristics stems from the radially decreasing density and irradiation. The density at $\tau \approx 1$ decreases moving outwards by a factor of ≈ 3.6 for interval C. However, the dominant factor is the decrease in burst flux. Across the radial zones, the average burst flux magnitudes drop by a factor of \approx 45 for time interval C. With decreasing burst flux, the degree of ionization decreases with distance from the neutron star, which enables stronger reflection features. Besides these features, a comparison of the reflected with the burst emission indicates the presence of a soft excess, soft emission not attributed to the burst emission (for further discussion, see Section 4.2).

The radially integrated reflection (black solid lines) and burst spectra (red dashed lines) for time intervals A, C, and E are shown in Fig. 5. The thermal radiation is not shown, but is included in the reprocessed emission. As already anticipated in Section 2, the evolution of reflection features with time stems mainly from the evolution of the irradiation, which gains in intensity and energy. The burst irradiation increasingly ionizes and heats the accretion disc,

increasing the amount of the soft excess. The advancing ionization weakens the emission lines. The emission lines are thus the strongest at the onset of the burst, as seen in the left panel. At $\approx 1~keV$, Fe L lines are visible. At $\approx 6.7~keV$, the spectrum features a recombination line of helium-like iron. We do not observe a Fe K α emission line at $\approx 6.4~keV$, because the disc is highly ionized during all time intervals. While Fe emission lines dominate the reflection spectrum, other ions such as C VI and O VIII produce emission lines at $\approx 0.37~and \approx 0.65~keV$. In time interval C (middle panel), the burst is brighter, ionizing the disc further and weakening emission lines, especially the Fe L lines at $\approx 1~keV$. An emission line at $\approx 7~keV$ by hydrogen-like iron appears next to the weakened helium-like line at $\approx 6.7~keV$. At the burst peak (right-hand panel), the disc is almost completely ionized. Emission lines weaken severely or, like the lines at $\approx 1~keV$, vanish altogether.

The weakening of emission lines translates into decreasing equivalent widths (EWs) over time (Fig. 6), calculated following Ballantyne & Ross (2002). When calculating the EWs, we neglect the diluting effect of the burst emission that is observed along with the reflection spectrum. We also ignore smearing due to disc rotation, which further decreases the EWs. On the other hand, we do not consider the disc beyond the 50 km radius, which will be less ionized, and therefore produce stronger emission lines. Longer simulations, where more of the simulated space reaches equilibrium, are needed to extend our calculations to a larger portion of the accretion disc. The Fe K lines at \approx 6.7–7 keV and the Fe L lines at \approx 1 keV are spaced closely together, respectively, so we report their respective cumulative EWs here. The Fe L lines (green dotted line) vanish during the burst ascent. Their cumulative EW decreases by \geq 99 per cent. The Fe K emission lines (dark red solid line) are the strongest at all times, despite their EW dropping by ≈ 90 per cent from the onset of the burst to its peak. C VI (orange dashed line) and O VIII (purple dot-dashed line) form the most stable emission lines. Their EWs decrease by \approx 75 per cent and \approx 80 per cent at interval E compared to interval A.

While the EWs decrease as the burst rises, the amount of soft excess increases (Fig. 7, black solid line). We calculated the percentage

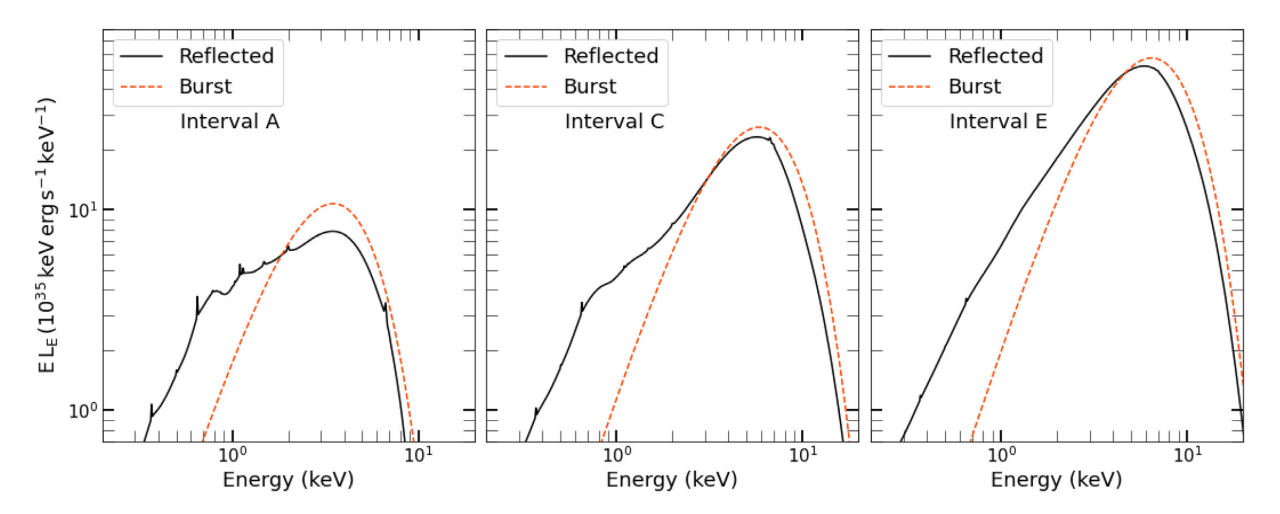


Figure 5. Radially integrated reflection spectra at different stages of the X-ray burst. The reflection spectra of the radial zones (Fig. 4) and the burst emission were integrated for each time interval. The burst (red dashed line) strengthens (equation 1, Fig. 1), increasingly ionizing and heating the accretion disc. The more intense irradiation gradually quenches any emission lines present in the reflection spectrum and increases the soft excess. The thermal radiation from the disc is not shown in the panels, but is included in the reprocessed emission.

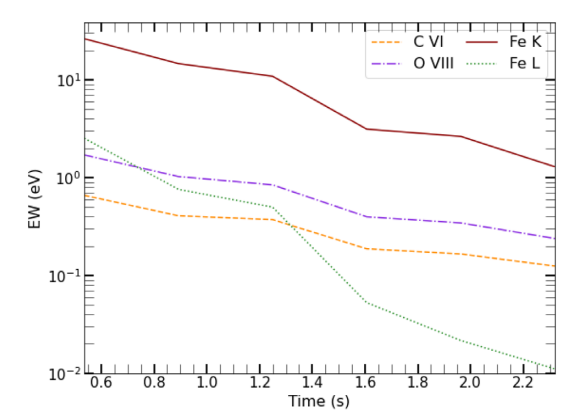


Figure 6. The EWs decrease over time due to the increasing ionization. The EWs were calculated following Ballantyne & Ross (2002) and only consider the reflection spectra. The Fe L lines (green dotted line) at $\approx 1~\rm keV$ vanish during the burst rise; their combined EW decreases by $\gtrsim 99~\rm per$ cent towards the burst peak. The Fe K (dark red solid line) lines remain the strongest ones throughout the burst ascent but weaken by $\approx 90~\rm per$ cent nevertheless. The C VI (orange dashed line) and O VIII (purple dot–dashed line) lines are more stable during the burst. Their EWs decrease by $\approx 75~\rm per$ cent and $\approx 80~\rm per$ cent between interval A and E, respectively.

of soft excess below 3 keV not attributed to burst irradiation as

$$S = \frac{\int_{E_1}^{E_h} \left[F_s(E) - F_{bb}(E) \right] dE}{\int_{E_1}^{E_h} F_s(E) dE} \times 100, \tag{5}$$

where $F_s(E)$ is the integrated reflection spectra emission (Fig. 5, solid black line), and $F_{bb}(E)$ the integrated burst emission at energy E (Fig. 5, dashed red line). The energies E_1 and E_h are $\approx 10^{-2}$ and ≈ 3 keV, respectively. The soft excess \mathcal{S} increases from ≈ 4 per cent from the burst onset to ≈ 38 per cent at the burst peak. The trend in soft excess is due to Compton scattering and bremsstrahlung processes. The increasing burst luminosity increases the mean burst photon energy during the burst rise, increasing the Compton scattering rate. In addition, the increasingly energetic photons heat the disc, producing a rising number of bremsstrahlung photons. These photons undergo further Compton scattering in the hot, low-density disc

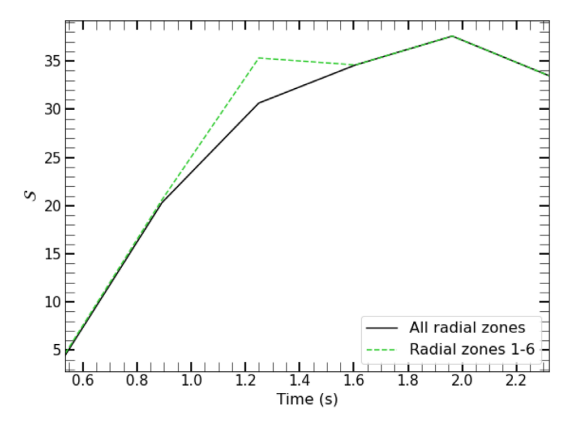


Figure 7. The percentage of soft excess <3 keV \mathcal{S} (black solid line, equation 5). The soft excess increases during the burst rise. The increasing burst luminosity (equation 1) heats the disc, which strengthens Compton scattering and bremsstrahlung rates. Structural disc changes past the burst peak reduce the soft excess in time interval F (see also Section 4.3). If the innermost radial zone 0 is neglected (green dashed line, Section 4.2), \mathcal{S} is larger compared to integrating over all radial zones (black solid line). The difference in \mathcal{S} exists up to time interval C; time intervals D–F do not have a radial zone 0.

surface on their way outwards. Some bremsstrahlung photons are thus upscattered and removed from the soft excess.

4 DISCUSSION

4.1 Implications for observations of X-ray bursts

As X-ray bursts brighten over the course of seconds, time-resolved spectroscopy of the burst ascent is challenging. In this section, we therefore compare our results to studies focusing on the burst tail. While we expect that the reflection spectrum in the burst tail will approximately retrace the evolution shown in Section 3 (Fig. 5), the burst tail will not be the exact reverse image of the burst rise. In the tail, the burst will continue to heat the disc and impact the disc geometry and thus its spectrum (Section 4.3). Longer simulations of

the disc-burst interaction lasting the entire burst are needed to predict the trends of observational properties more precisely. Nevertheless, we believe that our qualitative results should apply to many objects.

A frequently observed feature is a soft excess increasing with burst luminosity and has either been treated as a byproduct of an increase in the mass accretion rate or due to reflection (e.g. in't Zand et al. 2013; Worpel et al. 2013, 2015; Keek et al. 2018; Bult et al. 2019). The observed soft excess persists even when the model of the burst emission is allowed to diverge from a blackbody at low energies (Sánchez-Fernández et al. 2020). Our calculations show that reflection can produce a strong soft excess. Similar to observations, the strength of the modelled soft excess rises with burst luminosity in the burst ascent (Fig. 7). In fact, we find a soft excess starting from the onset of the burst, where the burst luminosity is still relatively low (Fig. 7). Hence, a reflection-induced soft excess could be a standard feature of X-ray bursts regardless of their burst luminosity.

The burst also affects emission line formation. In our calculations, the rising disc ionization due to the rising burst luminosity weakens emission lines considerably. At the burst peak, the high ionization of the accretion disc renders many of the initially present emission lines undetectable. The difficulty in observing emission lines for a highly ionized accretion disc agrees with simulation results (e.g. Keek, Wolf & Ballantyne 2016), and measurements of spectra without emission lines during a bright burst (e.g. Keek et al. 2018; Chen et al. 2019). The burst blackbody temperature impacts emission line formation as well. Iron K lines, for instance, require burst photons with energies >7.1 keV (Fabian et al. 2000). In our calculations, the burst blackbody temperature peaked at ≈1.6 keV (equation 2, Fig. 1), consequently producing relatively few burst photons with energies ≥ 7.1 keV (see Fig. 5, orange dashed lines), which, in combination with the high disc ionization, contributed to the weakness of the Fe K lines in the calculated spectra. X-ray bursts can have stronger Fe K emission lines since observations yield burst blackbody temperatures up to ≈3 keV (e.g. Hoffman, Lewin & Doty 1977; Ballantyne & Strohmayer 2004), corresponding to more photons above the 7.1 keV threshold. However, we still expect these emission lines to follow the trend of our calculated lines, and to weaken with increasing ionization, regardless of the burst blackbody temperature.

Despite different burst temperatures, our reflection calculations share similarities with the time-resolved studies of superbursts by Ballantyne & Strohmayer (2004) and Keek et al. (2014b). Ballantyne & Strohmayer (2004) studied a superburst of 4U 1820–30, and Keek et al. (2014b) examined a superburst of 4U 1636–536, both observed with *RXTE*. As both bursts declined, the degree of ionization decreased by more than a factor of 10. In our calculations of the burst rise, we similarly observe that the disc ionization increases with burst strength.

We expect more emission lines to form and strengthen during a burst with a smaller peak luminosity. As observed by Strohmayer & Brown (2002) and Keek et al. (2014a), we anticipate a Fe K α line at \approx 6.4 keV to form in a less ionized disc. With less ionization, we furthermore anticipate Fe L emission lines to strengthen. Previous burst observations detected an emission line at \approx 1 keV (e.g. Degenaar et al. 2013; in't Zand et al. 2013; Keek et al. 2017; Bult et al. 2019). This line has often been attributed to iron and could be a combination of the emission lines we observe. Other metals will form emission lines with lower ionization as well. With less ionization, we expect more emission line formation, especially at energies \lesssim 1 keV as simulated by Ballantyne (2004).

4.2 Impact of the retreating inner accretion disc radius

The burst interaction with the accretion disc affects the disc structure. PR drag drains the inner region of the accretion disc, causing the inner accretion disc radius to retreat (Fragile et al. 2020). Here, we discuss the impact of the retreating inner radius on the reflection spectrum.

We study the impact of the retreating accretion disc by comparing the soft excess of the total integrated reflection spectrum to the soft excess of the reflection spectrum only integrated over the fixed zones 1–6 (Fig. 7, green dashed line). For the time intervals A–C, which have the extra zone 0, the soft excess of the spectrum integrated only over zones 1–6 (green dashed line) is higher than the soft excess of the total spectrum integrated over zones 0–6 (black solid line). The greatest difference in $\mathcal S$ occurs in interval C, where $\mathcal S\approx 35$ per cent for the spectrum of zones 1–6 compared to $\mathcal S\approx 31$ per cent for the total spectrum.

The reason for the difference in $\mathcal S$ for time interval C lies in the high disc temperatures across the radial zones. In time interval C, the burst flux illuminating radial zone 0 is \approx 45 times greater than for radial zone 6. The stronger burst flux in radial zone 0 heats the disc more compared to in zone 6. At $\tau \approx 1$, the gas of radial zone 0 is \approx 2.2 times hotter than of radial zone 6. The hotter gas increases cooling process rates. Compton cooling is more active in particular, \approx 25 times higher for zone 0 than zone 6 at $\tau \approx 1$ for interval C, and upscatters the produced bremsstrahlung photons out of the soft excess. High disc temperatures thus cause high cooling rates, which reduces the soft excess.

Since the region closest to the neutron star receives the greatest amount of flux, it is subject to more disc heating. As disc heating affects the soft excess, the soft excess evolution could indicate the movement of the inner accretion disc. Little disc retreat amounts to a highly irradiated, hot zone close to the neutron star that emits less soft excess. Fig. 7 shows that the consequence of an inner, hot zone is a lower \mathcal{S} . A relatively small soft excess could therefore possibly point towards considerable disc heating and little disc retreat.

4.3 Impact of the inflating accretion disc

The heating of the accretion disc due to the burst causes the accretion disc to inflate (Fragile et al. 2020), as Fig. 8 shows. The six panels feature a segment of the upper surface (black solid line) at around $r \approx 40\,$ km for the time intervals A–F. The coloured dots and the corresponding colour bar show the burst flux magnitude per cell. The upper surface steadily rises, starting from time interval A (leftmost panel), even past the burst peak (interval F, rightmost panel). Simultaneously, the burst flux magnitudes at the upper surface in the shown segments increase.

The flux evolution results in the upper surface of time interval F being the most irradiated, with an average flux \approx 1.7 times higher than in interval E. Although interval F is just past the peak luminosity, interactions between the gas and radiation in the simulation lead to regions of high flux despite a slightly lower luminosity injected at the inner boundary. As a result of this large flux, the disc in interval F is heated to the point where the soft excess extends beyond 3 keV (see also Section 4.2), and $\mathcal S$ decreases to \approx 33 per cent (Fig. 7). The high ionization further reduces the EWs of the emission lines in this interval (Fig. 6).

Disc inflation will influence the overall contribution of reflection in observations. As Fig. 8 shows, the rising upper disc surface begins to slowly turn towards the neutron star, which increases the solid angle subtended by the outer radial zones. For instance, the solid angle subtended by radial zone 6 is $\approx 50\,\mathrm{per}$ cent larger in interval F

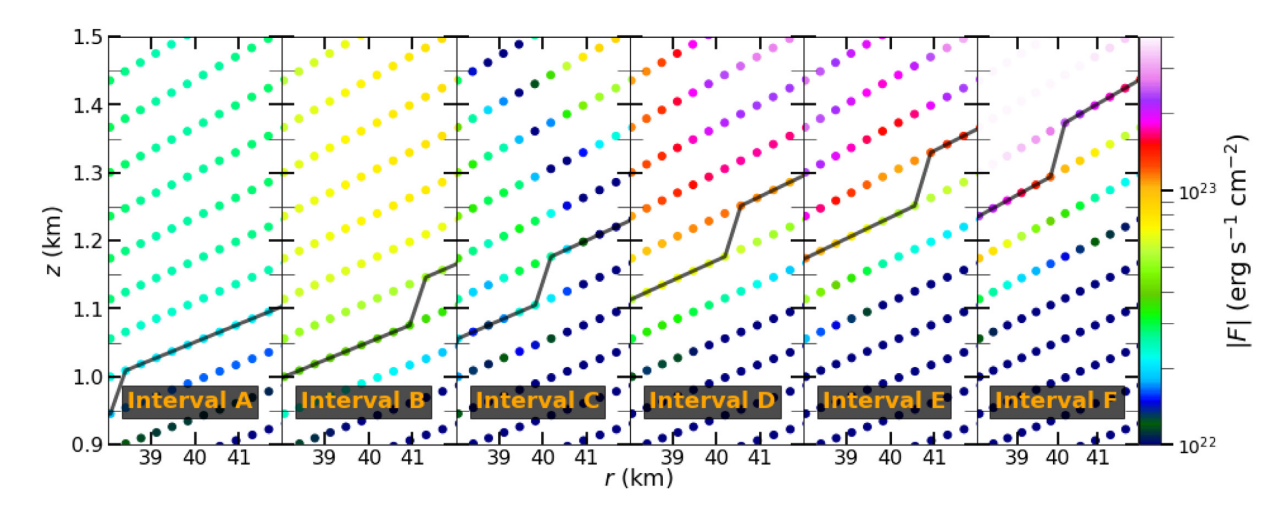


Figure 8. Segments of the upper surfaces at around $r \approx 40$ km for time intervals A–F. The upper surface (black solid line) rises steadily due to disc heating, starting from time interval A (leftmost panel). Simultaneously, the burst flux magnitude (dots, colour bar) increases. The rising disc surface remains highly irradiated throughout the burst, and leads to an ≈ 50 per cent increase in the solid angle subtended by the reflecting surface. The increase in solid angle enhances the importance of reflection at the burst peak.

compared to interval A. Disc regions further away from the neutron star will therefore be more irradiated and contribute more to the total reflected emission. Therefore, disc inflation will enhance the observed strength of highly ionized reflection close to the peak of the burst. As a result, despite the lack of emission lines, reflection is expected to provide a significant contribution to the total observed flux even past the peak of the burst.

5 CONCLUSIONS

Type I X-ray burst spectra often show signs of reflection. Prominent reflection features are iron emission lines and a soft excess (e.g. Degenaar et al. 2013; in't Zand et al. 2013; Keek et al. 2017, 2018; Bult et al. 2019; Chen et al. 2019). Tracing the reflection features over time during the tail of superbursts first indicated substantial changes in the accretion disc structure (Ballantyne & Strohmayer 2004; Keek et al. 2014b). These changes were recently simulated by Fragile et al. (2020). In this paper, we processed the simulation data of Fragile et al. (2020) to calculate the reflection spectra for six time intervals spanning the burst peak (Section 2). For each time interval, we divided the reflecting region into radial zones. For every zone, we determined vertical density profiles, the average burst and thermal fluxes, and their temperatures. We computed the reflection spectra for each time interval and radial zone and finally integrated them.

The emission lines in the calculated spectra weaken due to the increased ionization over the course of the burst rise (Section 3). While the calculated ionization evolution agrees with superburst observations (Section 4.1), the relatively low burst blackbody temperature combined with the high disc ionization in our calculations significantly limits the strength and types of emission lines we observe. Nevertheless, we expect observed emission lines to follow the calculated trend and weaken with increased ionization, regardless of the burst blackbody temperature.

We show that reflection is able to naturally produce a soft excess, which should be a standard feature of X-ray burst spectra. Our calculated soft excess is the product of Compton scattering and bremsstrahlung processes due to increasingly energetic photons heating the disc. The soft excess fraction evolves during the burst not only due to the unfolding burst but also because of the evolving disc structure; the drainage of the innermost disc region increases the

soft excess (Section 4.2), while disc inflation decreases the soft excess (Section 4.3). The observed soft excess will be a combination of an excess due to reflection and an increase in the persistent spectrum due to an enhanced mass accretion rate (Worpel et al. 2013, 2015). Disentangling these two effects will allow a deeper understanding of the accretion disc geometry.

Our work is a self-consistent prediction of a time-varying reflection spectrum and underlines the importance of studying dynamically resolved reflection spectra. The emission line evolution indicates the development of disc ionization and burst energy. Changes in soft excess could give insight into the disc geometry. To enhance the diagnostic capabilities of emission line features and the soft excess, their dependence on burst and disc characteristics must be known. Future work will probe the impact of burst and disc properties on the reflection spectrum.

ACKNOWLEDGEMENTS

The authors thank P. Bult, T. Güver, and the anonymous referee for helpful comments that improved the manuscript. PCF acknowledges support from National Science Foundation grants AST-1907850 and PHY-1748958.

DATA AVAILABILITY

The data underlying this article will be shared on reasonable request to the corresponding author.

REFERENCES

Ballantyne D. R., 2004, MNRAS, 351, 57
Ballantyne D. R., Ross R. R., 2002, MNRAS, 332, 777
Ballantyne D. R., Strohmayer T. E., 2004, ApJ, 602, L105
Ballantyne D. R., Ross R. R., Fabian A. C., 2001, MNRAS, 327, 10
Bult P. et al., 2019, ApJ, 885, L1
Cackett E. M. et al., 2010, ApJ, 720, 205
Chen Y. P. et al., 2019, J. High Energy Astrophys., 24, 23
Degenaar N., Miller J. M., Wijnands R., Altamirano D., Fabian A. C., 2013, ApJ, 767, L37
Degenaar N. et al., 2018, Space Sci. Rev., 214, 15

Ding G. Q., Chen T. T., Qu J. L., 2021, MNRAS, 500, 772

```
Fabian A. C., Iwasawa K., Reynolds C. S., Young A. J., 2000, PASP, 112,
1145
```

Fragile P. C., Ballantyne D. R., Blankenship A., 2020, Nat. Astron., 4, 541 Galeev A. A., Rosner R., Vaiana G. S., 1979, ApJ, 229, 318

Galloway D. K., Keek L., 2021, in Belloni T. M., Méndez M., Zhang C., eds, Astrophysics and Space Science Library. Vol. 461, Timing Neutron Stars: Pulsations, Oscillations and Explosions, Springer, Berlin, p. 209

García J., Kallman T. R., Mushotzky R. F., 2011, ApJ, 731, 131

García J. A., Sokolova-Lapa E., Dauser T., Madej J., Różańska A., Majczyna A., Harrison F. A., Wilms J., 2020, ApJ, 897, 67

Gendreau K., Arzoumanian Z., 2017, Nat. Astron., 1, 895

George I. M., Fabian A. C., 1991, MNRAS, 249, 352

Hoffman J. A., Lewin W. H. G., Doty J., 1977, ApJ, 217, L23

in't Zand J. J. M. et al., 2013, A&A, 553, A83

Inogamov N. A., Sunyaev R. A., 1999, Astron. Lett., 25, 269

Inogamov N. A., Sunyaev R. A., 2010, Astron. Lett., 36, 848

Keek L., Ballantyne D. R., Kuulkers E., Strohmayer T. E., 2014a, ApJ, 789, 121

Keek L., Ballantyne D. R., Kuulkers E., Strohmayer T. E., 2014b, ApJ, 797, L23

Keek L., Wolf Z., Ballantyne D. R., 2016, ApJ, 826, 79

Keek L., Iwakiri W., Serino M., Ballantyne D. R., in't Zand J. J. M., Strohmayer T. E., 2017, ApJ, 836, 111

Keek L. et al., 2018, ApJ, 855, L4

Lewin W. H. G., van Paradijs J., Taam R. E., 1993, Space Sci. Rev., 62, 223

Lightman A. P., White T. R., 1988, ApJ, 335, 57

Maccarone T. J., Coppi P. S., 2003, A&A, 399, 1151

Miller J. M., 2007, ARA&A, 45, 441

Nandra K., Pounds K. A., 1994, MNRAS, 268, 405

Norris J. P., Bonnell J. T., Kazanas D., Scargle J. D., Hakkila J., Giblin T. W., 2005, ApJ, 627, 324

Popham R., Sunyaev R., 2001, ApJ, 547, 355

Ross R. R., 1979, ApJ, 233, 334

Ross R. R., Fabian A. C., 1993, MNRAS, 261, 74

Ross R. R., Fabian A. C., 2005, MNRAS, 358, 211

Ross R. R., Weaver R., McCray R., 1978, ApJ, 219, 292

Rybicki G. B., Lightman A. P., 1986, Radiative Processes in Astrophysics. Wiley, New York Sánchez-Fernández C., Kajava J. J. E., Poutanen J., Kuulkers E., Suleimanov V. F., 2020, A&A, 634, A58

Speicher J., Ballantyne D. R., Malzac J., 2020, MNRAS, 499, 4479

Strohmayer T. E., Brown E. F., 2002, ApJ, 566, 1045 Szanecki M., Niedźwiecki A., Zdziarski A. A., 2021, ApJ, 909, 205

Walker M. A., 1992, ApJ, 385, 642

Worpel H., Galloway D. K., Price D. J., 2013, ApJ, 772, 94

Worpel H., Galloway D. K., Price D. J., 2015, ApJ, 801, 60

Xu Y., Harrison F. A., Tomsick J. A., Hare J., Fabian A. C., Walton D. J., 2020, ApJ, 893, 42

APPENDIX A: COMPARISON TO A CONSTANT DENSITY REFLECTION MODEL

Studies of X-ray bursts often rely on constant density reflection models (e.g. Ballantyne & Strohmayer 2004; Degenaar et al. 2013; in't Zand et al. 2013; Keek et al. 2014a, 2018; Bult et al. 2019). However, the density in real accretion discs will vary vertically within the reflection region. Here, we explore how the assumption of constant density would influence the derived reflection characteristics.

To quantify the impact, we ran calculations with a vertically constant $n_{\rm H}$ structure for all time intervals. Because most interactions will occur at $\tau \approx 1$, we selected the $n_{\rm H}$ values at this depth for each radial zone (Fig. 3). All other input values remained the same, and we computed the reflection spectra for each radial zone and time interval. As before, we integrated the reflection spectra of the radial zones to obtain the total reflection spectra per time interval.

Fig. A1 shows the difference of assuming a vertically constant $n_{\rm H}$ (blue dashed line) and the varying $n_{\rm H}$ profile taken from the simulation (black solid line) for time intervals C (left-hand panel) and E (right-hand panel). The spectra with the constant density assumption have a smaller soft excess at $\lesssim 2$ keV and stronger emission lines. These two differences result from a hot, low-density surface only present for the varying density profile. The surface of the constant density profile is denser, which makes cooling processes,

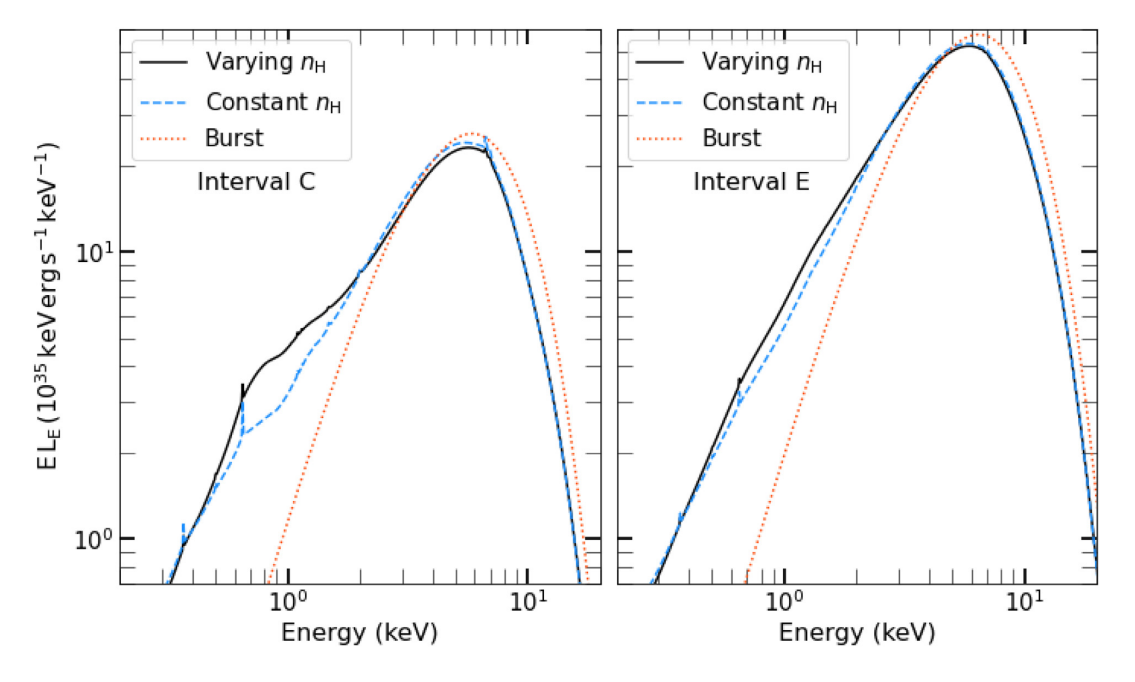
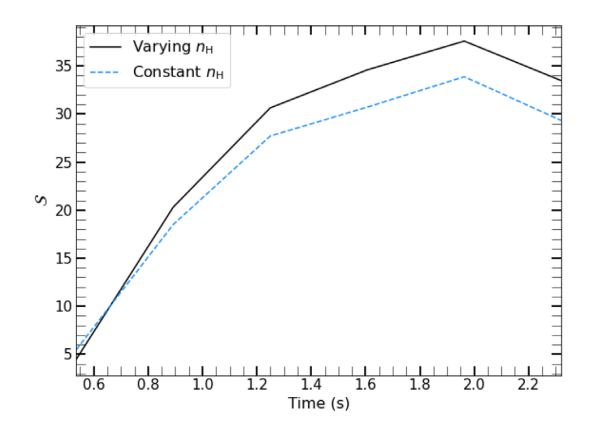


Figure A1. Same integrated reflection (black solid line) and burst spectra (orange dotted line) as in the middle and right-hand panel of Fig. 5, but overlaid with integrated constant $n_{\rm H}$ reflection spectra (blue dashed line). For the constant $n_{\rm H}$ reflection spectra, $n_{\rm H}$ is vertically constant in each radial zone. The constant density spectra have a smaller soft excess and stronger emission lines because cooling processes and line formation occur in denser disc regions in the constant than in the varying density case.



1744

Figure A2. Same \mathcal{S} as shown in Fig. 7, but overlaid with the soft excess percentage <3 keV of the constant density reflection model. If n_H is varying vertically per radial zone (black solid line), \mathcal{S} is up to \lesssim 1.1 times greater compared to a constant density reflection model (blue dashed line).

being two-body interactions, more efficient. Nevertheless, the lower soft continuum translates into a small $\mathcal S$ difference of \approx 28 per cent with the constant density versus \approx 31 per cent with the varying density in interval C (Fig. A2, blue dashed versus black solid line).

The emission lines with the constant density assumption are stronger because more metal ions are involved in line formation. For the varying density structure, ionization is concentrated in a thin, hot, low-density part of the disc. Line formation occurs at depths with higher metal ion density for the constant density assumption, which yields larger emission lines. For interval C, the O VIII line is stronger by a factor of $\approx\!2.5$ for a constant density slab. On average, with a constant density the EWs are greater by a factor of $\approx\!2$ in interval C.

The spectral shapes of the varying and the constant density models become more similar to each other as the burst rises, as shown by the spectra of interval E. The discrepancy in the soft excess between the two models is minor for high luminosities. At the peak of the burst, $\mathcal{S}\approx 34$ per cent for the constant density model and $\approx\!38$ per cent for the varying one. Moreover, Fig. A2 shows that \mathcal{S} for a varying density model is greater by a factor of $\lesssim\!1.1$ than for a constant density model during the burst ascent. Constant density reflection models are thus adequate tools to study the soft excess. Their performance to study emission lines is also acceptable, especially at the peak of the burst.

This paper has been typeset from a $T_EX/I \Delta T_EX$ file prepared by the author.